CHALMERS
UNIVERSITY OF TECHNOLOGY

Hydrogen embrittlement behaviour of AISI 321 stainless steel: Influence of temperature in tensile testing

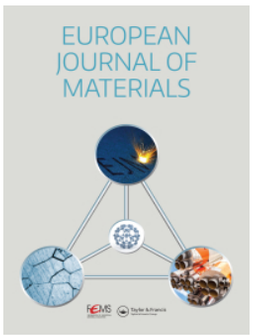

European Journal of Materials

ISSN: 2688-9277 (Online) Journal homepage: www.tandfonline.com/journals/tems20

Hydrogen embrittlement behaviour of AISI 321 stainless steel: Influence of temperature in tensile testing

Vishnu Anilkumar, Stefan Wanjura, Dirk Kulawinski, Frans Palmert, Johan Ahlström, Lars Nyborg & Yu Cao

To cite this article: Vishnu Anilkumar, Stefan Wanjura, Dirk Kulawinski, Frans Palmert, Johan Ahlström, Lars Nyborg & Yu Cao (2026) Hydrogen embrittlement behaviour of AISI 321 stainless steel: Influence of temperature in tensile testing, European Journal of Materials, 6:1, 2654905, DOI: 10.1080/26889277.2026.2654905

To link to this article: https://doi.org/10.1080/26889277.2026.2654905

Published online: 19 Apr 2026.

EUROPEAN JOURNAL OF MATERIALS
2026, VOL. 6, NO. 1, 2654905
https://doi.org/10.1080/26889277.2026.2654905

Taylor & Francis
by informa

STRUCTURAL MATERIALS

Hydrogen embrittlement behaviour of AISI 321 stainless steel: Influence of temperature in tensile testing

Vishnu Anilkumar[a,b], Stefan Wanjura[c], Dirk Kulawinski[c], Frans Palmert[d], Johan Ahlström[a], Lars Nyborg[a,b] and Yu Cao[a,b]

[a]Department of Mechanical Engineering, Chalmers University of Technology, Göteborg, Sweden; [b]TechForH2 Excellence Centre, Chalmers University of Technology, Göteborg, Sweden; [c]Siemens Energy Global GmbH & Co. KG, Mülheim an der Ruhr, Germany; [d]Siemens Energy AB, Finspång, Sweden

ABSTRACT

Gas turbines powered by hydrogen offer a promising route to cleaner energy production. However, the use of austenitic stainless steel AISI 321, a common material for fuel supply pipes presents challenges due to its susceptibility to hydrogen embrittlement, which is often linked to deformation-induced martensite formation and the presence of δ-ferrite. While deformation-induced martensite is suppressed above the alloy's M_d temperature, the embrittlement role of δ-ferrite at elevated temperatures remains unclear. In this study, slow strain rate tensile tests were conducted in both air and pressurized H_2 gas environments at room temperature (RT) and at 150 °C. Hydrogen embrittlement was observed at room temperature, as evidenced by a relative reduction in area of 0.44, whereas specimens tested at 150 °C exhibited no measurable embrittlement. Fractographic and microstructural analysis revealed that cracking of δ-ferrite phase boundaries at room temperature is associated with the formation of deformation-induced martensite. These findings demonstrate that hydrogen embrittlement in AISI 321 during tensile testing is primarily governed by the presence of deformation-induced martensite, and that δ-ferrite alone is insufficient to cause embrittlement at elevated temperatures. In addition, the effect of loading mode on HE behaviours is also discussed. The insight provided in this study is crucial for guiding material selection in hydrogen-fuelled gas turbines.

HIGHLIGHTS

- Slow strain rate tensile tests were performed in 4.6 MPa H_2 at RT and 150 °C.
- Hydrogen embrittlement was evident at RT but absent at 150 °C.
- Fractography at RT showed cleavage and delta-ferrite–associated secondary cracks.
- At 150 °C, fracture surfaces exhibited dimples and Ti(C,N) pull-outs.
- No deformation-induced martensite was detected at 150 °C.
- Highlights the role of martensite formation in hydrogen embrittlement under tensile loading.

ARTICLE HISTORY
Received 8 September 2025
Revised 12 November 2025
Accepted 30 March 2026

KEYWORDS
Hydrogen embrittlement; Slow strain rate tensile testing; Deformation-induced martensite; Austenitic stainless steels; Delta-ferrite

1. Introduction

Industrial gas turbines (IGTs) are widely used owing to high power generation capacity, fuel flexibility and high efficiency (Stefan et al., 2022). Gas turbines, traditionally fuelled by natural gas, are being upgraded to utilize pure hydrogen (H_2) or blends of H_2 and natural gas. This is because combustion of pure H_2 results in zero-carbon emission. In some IGTs, austenitic stainless steel 321 (hereafter, AISI 321) is used for fuel supply pipes due to its excellent intergranular corrosion resistance and weldability (Kumar & Shanmugam, 2018). Given their exposure to temperatures above 100 °C in service, the reliable operation of IGTs demand careful assessment of the mechanical performance of these components in high pressure gaseous H_2 environment at various temperatures.

Hydrogen embrittlement (HE) is a phenomenon in which the ductility and toughness of metallic materials is reduced with hydrogen uptake. It manifests as lowered macroscopic tensile ductility during tensile testing with the fracture surface exhibiting a non-ductile characteristic. The overall good HE

CONTACT Yu Cao yu.cao@chalmers.se Department of Mechanical Engineering, Chalmers University of Technology, Göteborg, Sweden

resistance of stable austenitic stainless steels due to slow hydrogen diffusion, qualifies them for relevant applications (Liu et al., 2023). However, metastable grades like AISI 321 are regarded as susceptible to HE at room temperature (RT), where the formation of deformation-induced martensite (DIM) has been found to play a primary role (Huang et al., 2022; Jürgensen et al., 2024; Rozenak, 1990; Rozenak & Eliezer, 1983; Xiuqing et al., 2021). Compared to austenite, martensite exhibits a higher hydrogen diffusion rate but lower hydrogen solubility. This promotes hydrogen accumulation along DIM phase boundaries, increasing the susceptibility to cracking in these regions (Imade et al., 2008; Zhang et al., 2010). The amount of DIM follows an exponential decay with temperature (Grosse et al., 2006). Martensite formation is reduced above the M_{d30} temperature, defined as the temperature at which 50% of austenite transforms into martensite under 30% true plastic strain. Above the alloy's M_d temperature, martensitic transformation becomes unfavourable (Jain & Varshney, 2024). In 300-series austenitic stainless steels with low-nickel content, alloys with $M_{d30} > -80\,°C$ exhibit greater susceptibility to HE than those with $M_{d30} < -80\,°C$, indicating a positive correlation between lower M_{d30} values and improved HE resistance (Izawa et al., 2019). As DIM is reported to be dominant factor contributing to HE, reduced martensite formation above M_{d30} temperatures such as in AISI 304 L leads to enhanced resistance (Lee, 2016).

However, contribution of delta-ferrite (δ-ferrite) to HE has received little focus. This is important as a few percent of δ-ferrite is common in solution annealed low nickel alloyed austenitic stainless steels (Buckley & Hardie, 1993; Graham & Lorenz, 2018). δ-ferrite has a BCC structure, which facilitates a rapid hydrogen diffusion in comparison to austenite (Frappart et al., 2010; Lee et al., 2020). This phase is stable at temperatures where DIM is not favoured. The difference in hydrogen diffusion between δ-ferrite and austenite leads to accumulation of hydrogen along the phase boundaries (Choi et al., 2024). Secondary cracking along δ-ferrite boundaries has been observed on the fracture surfaces of solution- annealed AISI 321 tested at RT in H_2 after thermal precharging and tensile testing in ambient environment (Jürgensen et al., 2024). δ-ferrite boundary cracking was also observed for AISI 321 after tensile testing with in-situ electrochemical hydrogen charging at RT (Xiuqing et al., 2021). Similarly, AISI 304 Austenitic stainless steel containing high δ-ferrite content showed greater HE susceptibility compared to the one free of δ-ferrite. An increase in δ-ferrite volume fraction was found to slightly increase the sensitivity to HE at RT (Buckley & Hardie, 1993). However, the improvement in HE resistance for the AISI 304 free of δ-ferrite was minor at RT, compared to AISI 304 rich in δ-ferrite (Bao et al., 2021).

While the presence of δ-ferrite is known to negatively impact HE resistance in solution annealed microstructures, the role of δ-ferrite alone remains unclear from existing studies. Most studies to date have focussed on performance at RT where formation of DIM occurs. Investigation at high temperatures is rare. Considering the applications of AISI 321 in gas turbines, validating the material performance at high temperatures is important. This study focusses on the less known effects of temperature on hydrogen embrittlement of AISI 321. A δ-ferrite containing AISI 321 is thermally precharged and in-situ tensile tested in 4.6 MPa H_2 both at RT, where DIM is expected, and at 150 °C, where DIM is not expected. The requirement of DIM transformation for embrittling δ-ferrite boundaries during tensile testing in H_2 has been discussed. This study aims to improve the understanding of the respective influence of DIM and δ-ferrite on the HE susceptibility, thus aiding the development of materials selection criteria for metastable austenitic stainless steels for applications involving exposure to high-temperature and high-pressure H_2 gas.

2. Experimental methods

2.1. Material and hydrogen charging

A commercial grade hot-rolled AISI 321 in solution annealed condition (1050 °C for 1 hour with air-quenching) was used in this study. The chemical composition of the as received material is listed in Table 1.

Tensile test bars were machined from a solution-annealed, hot-rolled plate in transverse direction and prepared according to ASTM E8/E8M-22. The gauge section was 30 mm in length and 6 mm in

Table 1. Chemical composition of the as received AISI 321 in wt. %

Elements	C	Mn	Si	Cu	Ni	Cr	Ti	Co	N	Fe
Wt.%	0.042	1.80	0.43	0.44	9.01	17.39	0.29	0.14	0.013	Bal

diameter. Thermal hydrogen precharging (grade 5.0) was performed in an autoclave at 350 °C and 4.6 MPa for 672 hours (~ 28 days) to approach through-thickness saturation. After charging, specimens were cooled in hydrogen to room temperature and stored at - 20 °C prior to testing. Total hydrogen content was measured by melt extraction using Bruker Galileo G8 on coupons taken from the grip ends. It was found that the concentration increased from 3.5 to 21.5 wt.ppm after charging.

2.2. Mechanical testing

Tensile tests were conducted at a strain rate of 1 x 10^{-5} (1/s) in-situ under 4.6 MPa H_2 at both RT and 150 °C until fracture. The test temperature of 150 °C was expected to be above the alloy's M_d temperature, which is the maximum temperature for deformation induced martensite transformation. It also corresponds to the maximum temperature allowable in the autoclave system. For the 150 °C tests, specimens were mounted in the test chamber, which was then pressurized to 4.6 MPa H_2 and subsequently heated to 150 °C before loading. Although hydrogen solubility in austenite decreases at 150 °C relative to the 350 °C pre-charging condition, the overall hydrogen loss during the tensile test is expected to be minimal. This can be explained as follows. At 150 °C, the diffusivity D of hydrogen in austenite remains relatively low on the order of ~10–13 m^2/s) (Marchi, 2005). The characteristic diffusion distance ($x = \sqrt{Dt}$) is estimated to be on the order of ~70 µm for a test duration t of ~13-15 hours, which is negligible compared to the 6 mm specimen diameter. Furthermore, the specimen remains under 4.6 MPa H_2 during testing, which helps to offset the hydrogen loss at 150 °C. Reference tests in air were also conducted at RT and 150 °C on the as-received material. Two replicate tensile tests were performed for each condition. The ductility was evaluated in terms of the area reduction (RA) at the fracture point using the Equation (1)

$$RA = \left(A_0 - A_f\right) / A_0 \times 100\% \quad (1)$$

where A_0 is the original cross section area and A_f is the area after fracture, which was measured by outlining from the image of fracture surface taken from a scanning electron microscope using open-source ImageJ software (Schindelin et al., 2012).

2.3. Microstructural characterization

The initial microstructure of as-received material was investigated using a Zeiss Gemini 450 scanning electron microscope (SEM) equipped with energy dispersive X-ray spectroscopy (EDS) (Oxford Analysis) and electron backscatter diffraction (EBSD) (Oxford, Symmetry). Fracture surfaces were inspected at an accelerating voltage of 5 kV and a probe current of 500 pA. For EDS, the probe current was increased to 1.5 nA. For post-mortem studies, the fractured specimens were sectioned along the longitudinal (loading) axis using a Buehler Isomet slow speed cutter with a diamond blade. The sections were mounted, ground with silicon carbide (SiC) foils from P1200 to P4000 and then electrochemically polished in a Struers Tegrapol polisher using Struers A3 electrolyte at 26 V for 30 seconds. Electron backscatter diffraction was performed with a step size of 0.15 µm over areas of ~ 0.12 mm^2 for phase quantification, while for classifying delta-ferrite and DIM near the crack a step size of 0.03 µm was used. All measurements were performed at an accelerating voltage of 20 kV with a probe current of 12 nA and a working distance of 7–8 mm. The EBSD data evaluation was performed using open source MTEX toolbox (version 6.0.0) in MATLAB® (Bachmann et al., 2010). Differentiation and quantification of deformation-induced martensite and δ-ferrite were performed on the EBSD phase maps using the "Classify" mode in AztecCrystal software. Image quality (IQ) metrics such as band contrast, band slope, and mean angular deviation (MAD) and grain morphology

were used to distinguish martensite from δ-ferrite. Phases were then confirmed by manual selection, while zero solutions and the austenite phase were protected to avoid misclassification. Due to the poor IQ metrics of large-area (0.12 mm^2) EBSD maps resulting from extensive plastic deformation in the air-tested specimens at room temperature, phase classification could not be performed with sufficient confidence and was therefore omitted. Hardness measurements according to ASTM E92-17 (Vicker's) were performed on the gage section of fractured tensile specimens away from the neck zone using a Struers DuraScan hardness tester. A total of 200 indents were made using HV 0.1 with 10 seconds dwell time for each indentation.

3. Results

3.1. Initial microstructure

The specimen extraction direction and the microstructure of the as-received material from two different planes are shown in Figure 1. In the solution annealed condition, AISI 321 consists primarily of an austenitic matrix containing Ti(C,N) precipitates and BCC structured δ-ferrite distributed along the rolling (Figures 1a and 1b) directions of the hot-rolled plate. The EDS elemental maps of a representative precipitate (Figure 1c) reveal enrichment in titanium, carbon, and nitrogen, confirming its identity as Ti(C,N).

3.2. Tensile testing

Tensile tests (two tests in each condition) were conducted on hydrogen precharged specimens in H_2 atmosphere at RT and 150 °C, with reference tests performed in air. The tensile curves in Figure 2 were cut at maximum stress. Under the same testing condition, the deviation was negligible for the duplicate specimens. In all cases, the steel exhibited continuous yielding behaviour and strain hardening.

The relative reduction of area (RRA) is a ratio of area reduction in H_2 and in air, as defined in Equation (2).

$$RRA = RA_{Hydrogen} / RA_{Air} \tag{2}$$

where $RA_{Hydrogen}$ denotes the reduction of area measured from samples fractured under hydrogen exposure, while RA_{Air} corresponds to the reduction of area obtained from samples fractured in air.

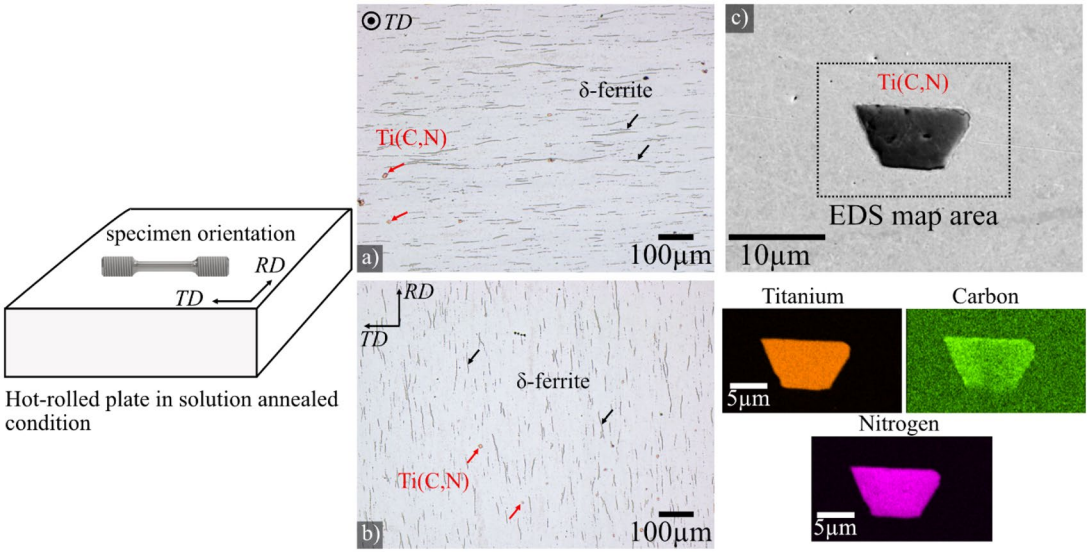

Figure 1. Microstructure of as-received AISI 321 stainless steel from (a) plane perpendicular to transverse direction (TD), and (b) plane defined by TD and rolling direction (RD), showing delta-ferrite and Ti(C,N); (c) EDS map of Ti(C,N).

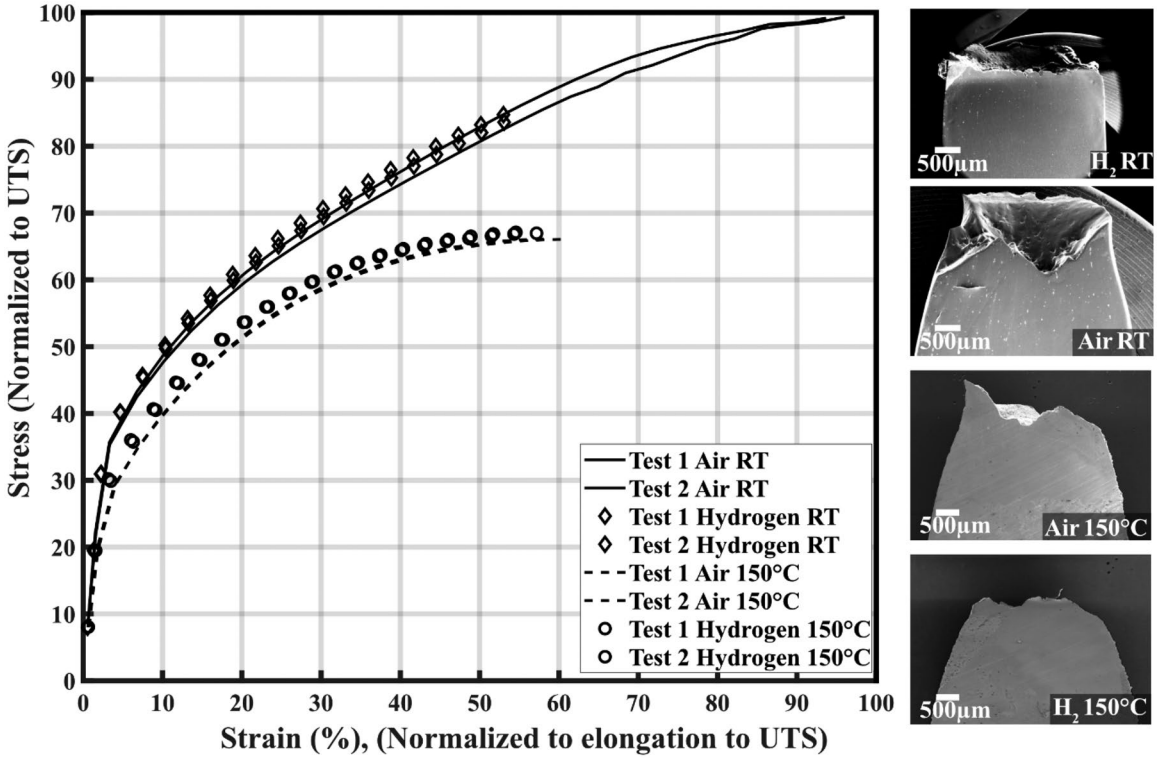

Figure 2. Normalized engineering stress-strain curve till ultimate tensile strength (UTS) at room temperature and 150 °C in air and H_2 (left); longitudinal cross sections of fracture surfaces tested at room temperature and at 150 °C are also shown (right).

Table 2. Reduction of area after tensile testing

Environment	Temperature	Reduction of area (RA) (%)	Relative Reduction of Area (RRA)
Air	Room	65.4 ± 0.57	0.44
Hydrogen	Room	29.15 ± 2.19	
Air	150 °C	74.55 ± 0.07	0. 98
Hydrogen	150 °C	73.25 ± 2.19	

The relative reduction of area helps to understand the influence of hydrogen on macroscopic tensile ductility. As a measure of HE susceptibility, an RRA value of "1" indicates no influence of hydrogen (Izawa et al., 2019). The reduction of area (RA) and RRA are given in Table 2. At room temperature, hydrogen was not found to influence either yield strength or strain hardening rate ($d\sigma/d\varepsilon$), as seen from Figure 2. In comparison to the test in air, however, tensile strength was decreased in H_2 tested specimens. Premature failure was noticeable with lower uniform elongation at maximum stress. In addition, area reduction at fracture was decreased significantly from 65.4 ± 0.57 to 29.15 ± 2.19 (%), indicating considerable embrittlement induced by hydrogen uptake. The noticeably lower necking in specimen tested in H_2 in comparison to air is shown on the upper right of Figure 2. This confirms that the premature fracture was indeed influenced by the hydrogen uptake.

When the testing temperature was increased to 150 °C, material softening was observed in both samples tested in air and H_2. This was accompanied by a reduction in yield strength, tensile strength, strain hardening, and uniform elongation compared to specimens tested at RT. On the contrary, reduction of area was increased, especially in H_2 tested specimens, as seen in Table 2. Notice, the total reduction of area is the sum of uniform and non-uniform ones in the neck region, whereas the latter is generally dominant. Significantly improved reduction of area at 150 °C indicated much higher local deformation capability. Interestingly, the influence of H_2 on tensile behaviour was rather small at 150 °C. The material behaved similarly in both environments with ignored change in strength and no drop in uniform elongation at this temperature. As presented in Table 2, the lower RRA value of

0.44 in H_2 tested specimens at RT meant hydrogen embrittlement was present. On the contrary, RRA value of 0.98 measured from the specimens at 150 °C indicated that hydrogen embrittlement was almost eliminated at this temperature.

3.3. Fractography

3.3.1. Room temperature tensile test

The fracture surfaces of specimens tested at room temperature were examined to understand the influence of hydrogen, as shown in Figures 3 and 4. The specimen tested in air featured a ductile fracture with dimples and pull outs of Ti(C,N) precipitates (Figure 3b), owing to strength mismatch. The parallel cracks visible on fracture surfaces are "streaks" of Ti(C,N) precipitates (Figures 3a and 3b). In comparison, the specimen tested in H_2 exhibited a hydrogen-assisted cracking zone and plastic

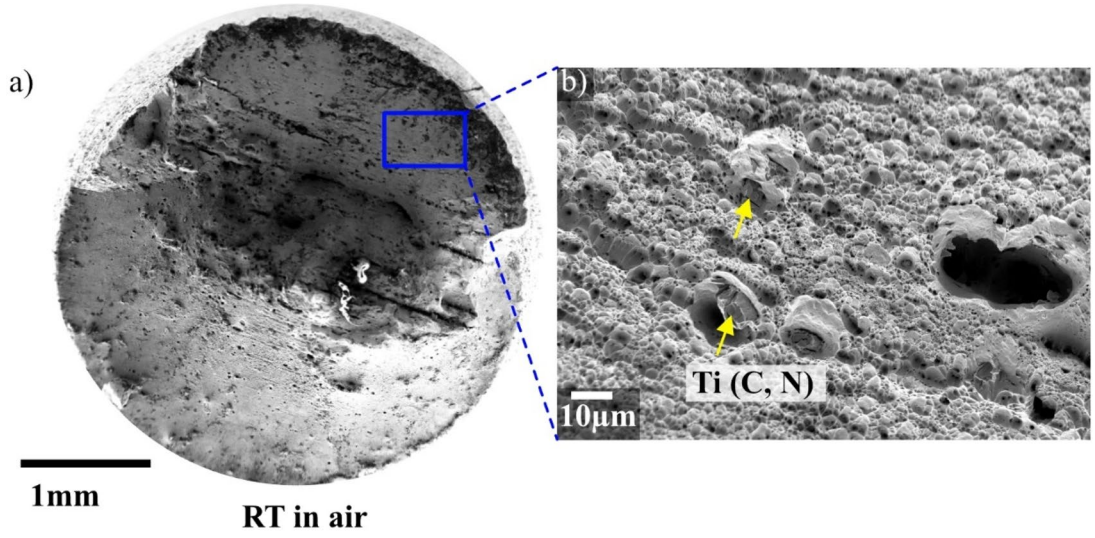

Figure 3. Fracture surface in air at room temperature; (a) overall fracture surface; (b) ductile features present.

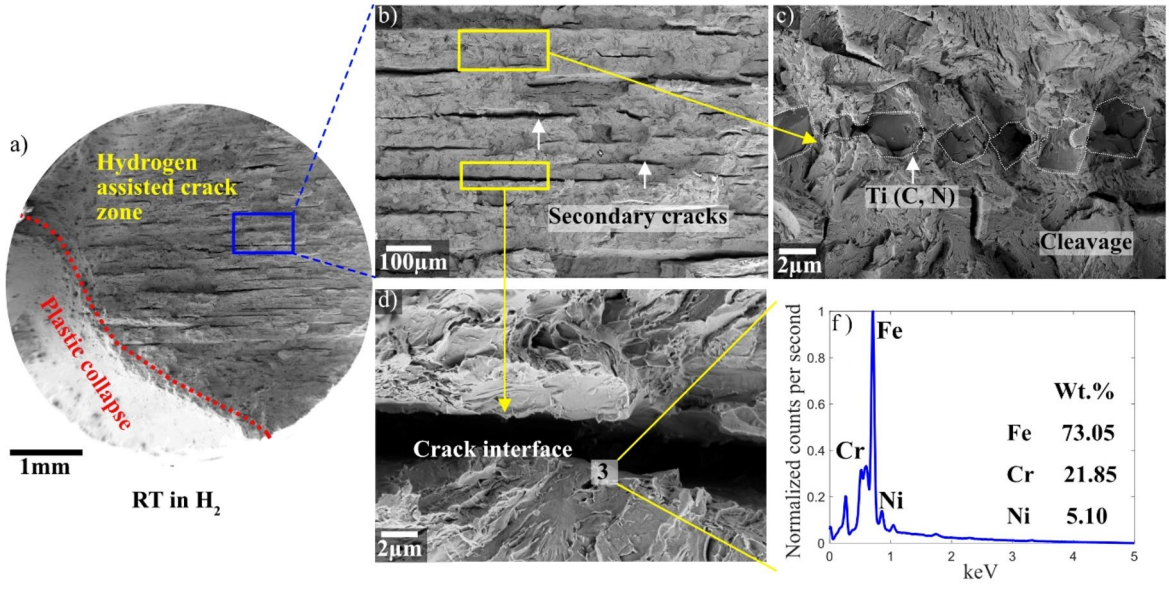

Figure 4. Fracture surface in H_2 at room temperature; (a) overall fracture surface (b) secondary cracking; (c) magnified view of region in (b), showing cleavage around Ti(C,N); (d) and (f) magnified view of crack interface and EDX point analysis of crack in (d).

collapse as marked in Figure 4a. The former presented a flat fracture surface resulted from a rapid crack propagation, whereas the plastic collapse led to the observed ductile dimples.

At higher magnification, the hydrogen-assisted cracking zone shows a transgranular quasi-cleavage, accompanied by secondary cracking when tested in H_2 at RT, as indicated by the white arrow in Figure 4b. This was different from ductile fracture in air. Cleavage was also observed around Ti(C,N) precipitates, as shown in Figure 4c. This contrasted with the dimple formation and the pull-out of Ti(C,N) seen under air conditions (Figure 3b). The secondary cracks are located along the δ-ferrite boundaries, as confirmed in Figure 4d and by the EDX spectrum in Figure 4f. Point analysis revealed chromium enrichment and Nickel depletion, consistent with the presence of δ-ferrite (Sadeghi et al., 2021).

To understand secondary cracking seen in Figure 4b, SEM imaging and EBSD were performed on longitudinal cross sections close to the fracture zone, as illustrated in the schematic of Figure 5a. The crack found on the fracture surface was observed to extend into the underlying material, further confirming that crack propagation is favoured along the delta-ferrite boundaries (Figure 5b). The alignment of crack with the loading axis likely results from the preferential growth of crack fronts into delta-ferrite regions that are oriented to the loading direction (see Figures 1a and 1b). Additionally, EBSD mapping performed in a neighbouring region revealed the presence of martensite along the phase boundaries of δ-ferrite (Figures 5c and 5d).

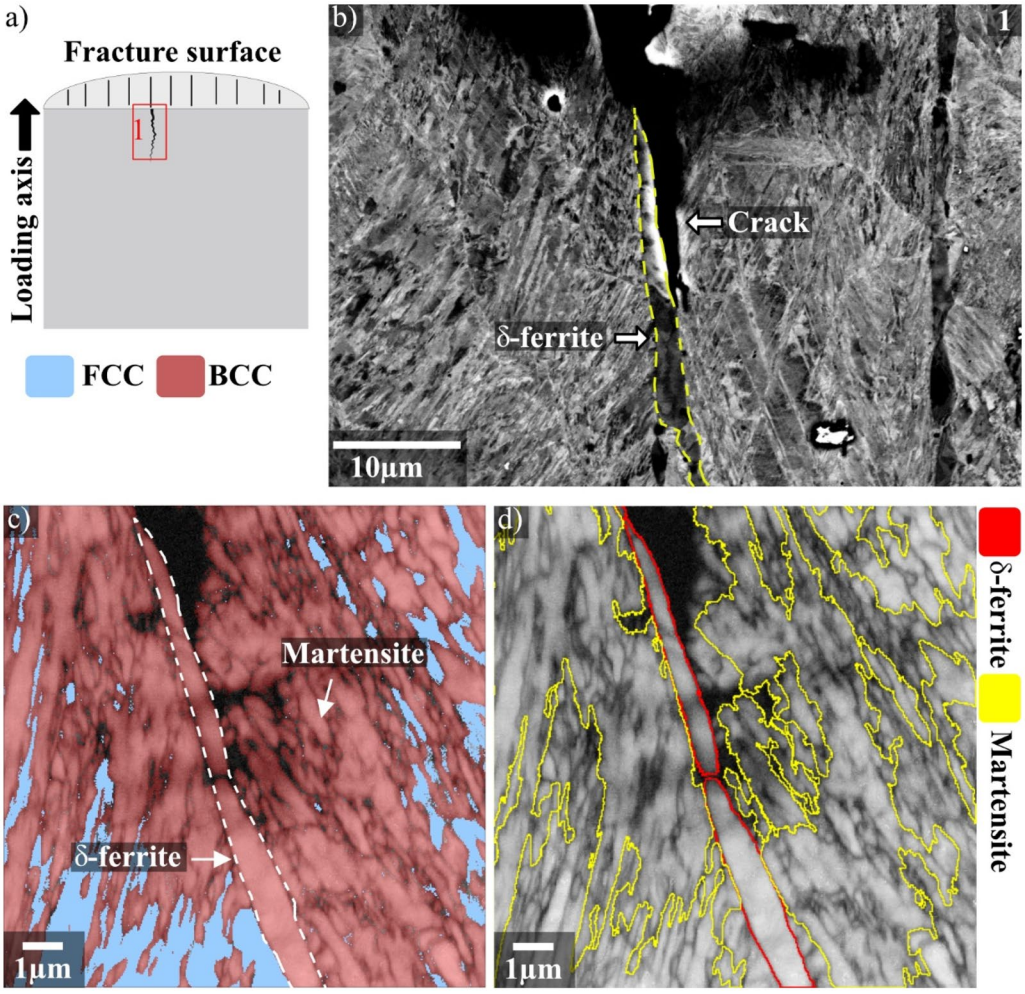

Figure 5. (a) Schematic of longitudinal cross-section (parallel to tensile loading axis) of the specimen tested in H_2 at room temperature. (b) Crack formation along δ-ferrite interface; (c) EBSD phase map revealing the presence of martensite along the phase boundaries of δ-ferrite (different region than (b)). (d) Identifying martensite and delta-ferrite using "Classify" tool in AztecCrystal; here difference in grain morphology between delta-ferrite and martensite is used for differentiating the two phases.

3.3.2. Elevated temperature tensile test

The overall fracture surface of specimens tested at 150 °C in air and in H_2 is shown in Figures 6a and 6c. The ductile nature of the fracture featuring dimples was visible in both specimens. In addition, carbonitride pull-outs are more prominent at this temperature, as shown in Figures 6b and 6d, compared to RT (refer Figure 3b). It seemed that hydrogen had no influence on the nucleation and growth of micro-void, as observable from the fracture surfaces (Figures 7a and 7b). A total of 5 images were used from different regions of fracture surfaces to draw this conclusion. It should be

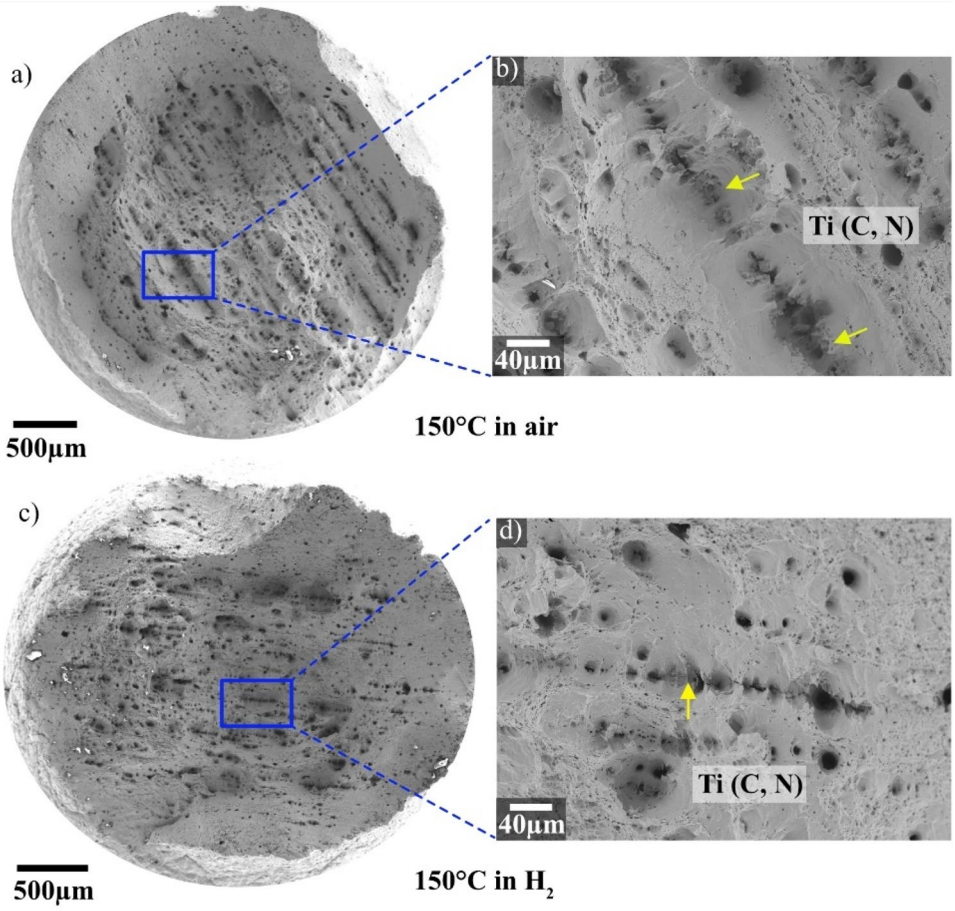

Figure 6. Overall fracture surface in air (a) and in H_2 (c) at 150 °C; Cracking of Ti(C,N) streaks in air (b) and in H_2 (d) at 150 °C.

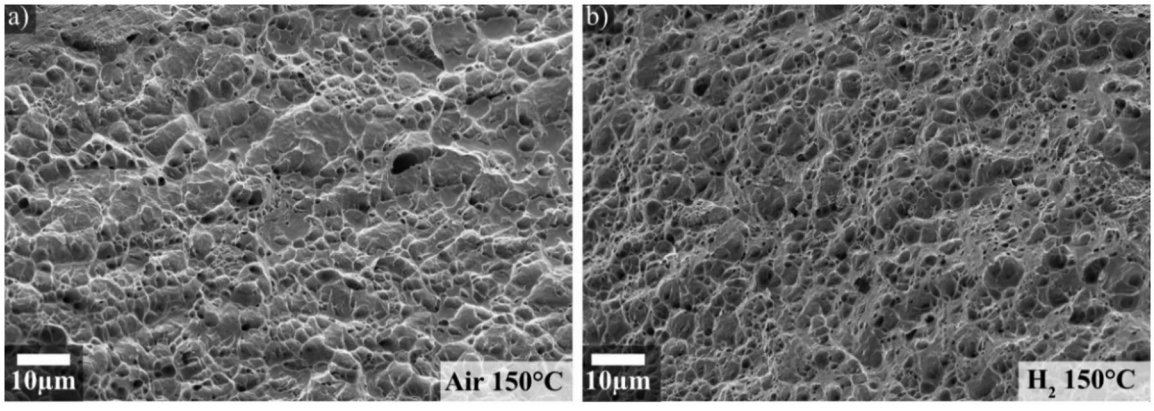

Figure 7. Dimples observed on the fracture surfaces of specimens tested in air (a) and H_2 (b) at 150 °C.

noted that some regions exhibited finer and denser dimples in H_2 tested specimens. However, in general, the effect of hydrogen was insignificant at this temperature.

3.4. Influence of phases

The role of deformation-induced martensite in HE susceptibility of AISI 321 has been widely studied. It is known that higher temperature decreases the susceptibility towards HE (Huang et al., 2022; Lee, 2016; Rozenak, 1990; Rozenak & Eliezer, 1983; Xiuqing et al., 2021). However, in the presence of δ-ferrite, the influence of martensite on secondary cracking along the δ-ferrite interfaces is less clear. To clarify this, tensile testing was performed at 150 °C where martensite transformation is not favoured. To further understand the effect of temperature, EBSD analysis on the cross-section parallel to the loading direction under different conditions was performed and the phase maps overlaid on band contrast images are exhibited in Figure 8.

The BCC phase observed in Figures 8a and 8b comprises of both δ-ferrite and martensite. The largest phase fraction of BCC was found in the specimen tested in air at RT, indicating extensive formation of DIM, as the amount of δ-ferrite was supposed to be constant. The steel was embrittled by hydrogen at room temperature, and the tensile ductility in terms of RA was decreased from 65.4 ± 0.57 in air to 29.15 ± 2.15 (%) in H_2. This premature fracture reduced the amount of martensite content, as seen in Figures 8a and 8b, attributed to the decrease in total plastic strain from hydrogen-induced ductility loss (Kim et al., 2016). Here, an elongated nature of the BCC phase was seen. In contrast to room temperature testing, the formation of DIM was not observed at 150 °C, as revealed in Figures 8c and 8d. Here, the BCC phase corresponds exclusively to δ-ferrite, which can be confirmed by: (i) its distinct morphology compared with DIM (see Figure 1a and Figure 5d), and (ii) the EBSD band-contrast maps overlaid with the phase map, in which austenite grain boundaries remain sharp and free of the contrast degradation typically associated with martensite transformation.

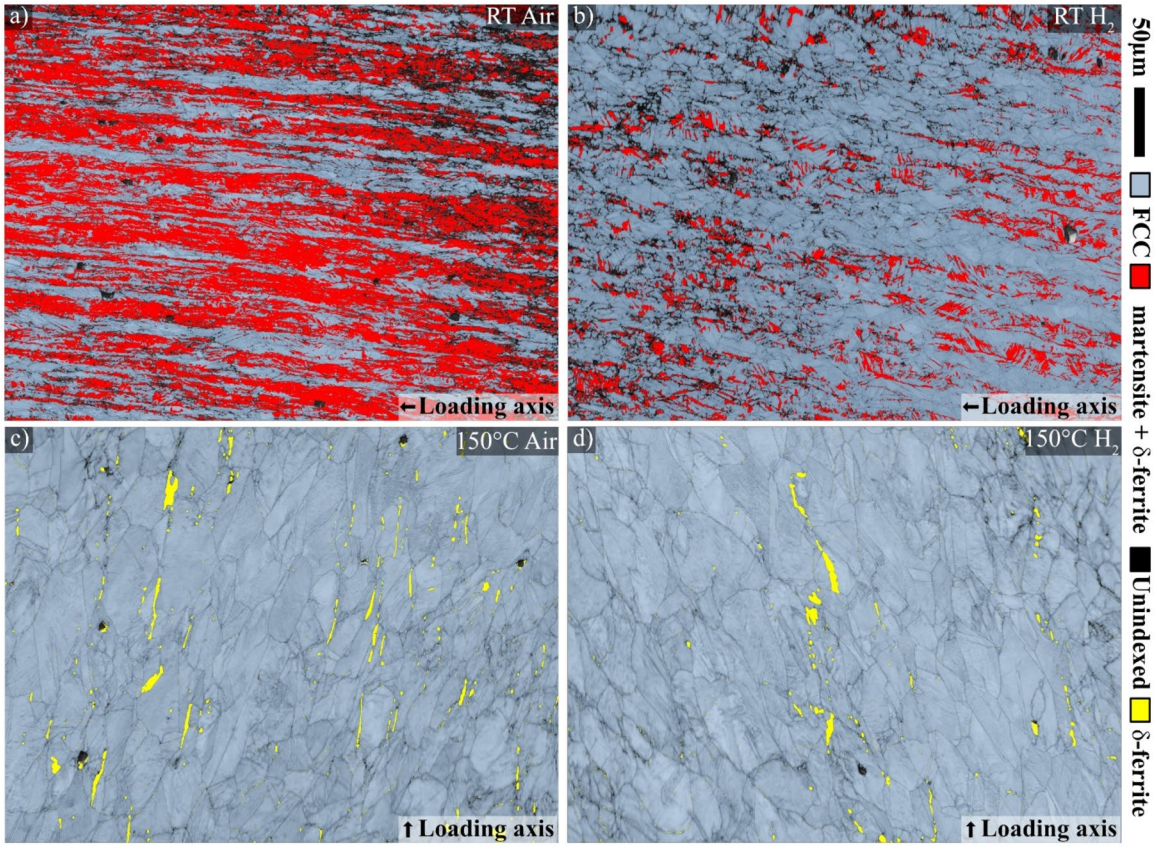

Figure 8. EBSD phase maps + band contrast image on the cross section parallel to the loading direction in air (a) and H_2 (b) at RT; in air (c) and H_2 (d) at 150 °C.

The clearer band contrast arises from its lower strain relative to no martensite at 150 °C. Note the different directionality of the δ-ferrite bands in Figures 8c and 8d compared to BCC phase (martensite + δ-ferrite) in Figures 8a and 8b was merely due to the difference in alignment of the surfaces in EBSD.

The hardness measurements (Table 3) within the gauge section but away from neck zone after tensile testing were consistent with these observations. Compared to the hardness of the as received steel (188.55 ± 10.5 HV), the hardness after testing was increased under all conditions due to strain hardening. The specimens tested in air at room temperature showed the highest hardness (390.8 ± 34.5 HV), reflecting the largest martensite fraction. Lower hardness from the specimen tested in hydrogen at room temperature was due to reduced martensite formation caused by premature fracture. In contrast, the specimens tested at 150 °C exhibited hardness values lower than those tested at RT, confirming the absence of martensite formation at this temperature, irrespective of testing environment.

4. Discussion

Hydrogen embrittlement under tensile testing of metastable austenitic stainless steels including AISI 304 and AISI 321 has been widely studied (Bao et al., 2021; Choi et al., 2024; Huang et al., 2022; Rozenak & Eliezer, 1983; Wang et al., 2014; Xiuqing et al., 2021; Yun et al., 2024). The presence of δ-ferrite has been found to accelerate HE and promote secondary cracking. However, these findings are based on studies performed at room temperature, where martensite formation is favoured. It remains unclear whether martensite is required for δ-ferrite boundary cracking or can δ-ferrite alone trigger HE under tensile loading. To understand this, high temperature testing in H_2 environment is of interest where martensite formation is not favoured. In this regard, the study aims to understand the hydrogen embrittlement of AISI 321 under tensile testing at RT, and 150 °C. It is found that HE susceptibility defined as RRA is 0.98 at 150 °C in contrast to 0.44 at RT, indicating a significantly increased resistance to HE at 150 °C. Additionally, the absence of secondary cracking along the δ-ferrite phase boundaries at this temperature indicates the necessity of DIM formation for causing secondary cracks along these boundaries under tensile loading.

Tensile testing in H_2 atmospheres at RT has been found to induce transgranular quasi-cleavage, and secondary cracking along δ-ferrite interface boundaries (Figure 4a). However, this observation is not present in specimen tested at 150 °C in H_2 atmosphere (Figures 6c and 6d). It is well known that hydrogen has high solubility but low diffusivity in austenite, while low solubility but high diffusivity in martensite. As a result, the formation of DIM from austenite at RT creates hydrogen-super-saturated martensite with accumulation of excess hydrogen above the solubility along the phase boundaries which become prone to transgranular quasi-cleavage (Wang et al., 2014; Wang et al., 2018; Zhang et al., 2013a; Zhang et al., 2013b). This explains the characteristic quasi-cleavage morphology on the fracture surface. Interestingly, DIM is formed preferentially in austenite adjacent to the δ-ferrite- interfaces, as seen in Figures 5c and 5d. This behaviour is likely associated with heterogeneous partitioning of plastic strain between δ-ferrite and austenite. Note the softer austenite must accommodate a larger share of local plastic strain, thereby promoting strain induced martensite transformation (Fu et al., 2012; Lee et al., 2021). In the presence of hydrogen, such localized DIM formation can facilitate interfacial decohesion, consistent with the boundary cracking as shown in Figure 4a. Similar fracture surfaces with transgranular cleavage were observed in metastable AISI 321 and AISI 304 after tensile testing at RT (Jürgensen et al., 2024; Marchi et al., 2010). Jürgensen et al. (2024) correlated this to the presence of DIM based on fracture surface analysis in AISI 321. Marchi et al. (2010) observed long parallel cracks on the fracture surface of AISI 304. However, no

Table 3. Hardness measurements (Vicker's HV0.1) for as-received and tested specimens (away from the neck zone).

Condition	Hardness
As received	188.5 ± 10.5
Air (RT)	390.8 ± 34.5
Air (150 °C)	280.3 ± 10.5
H_2 (RT)	330 ± 31.6
H_2 (150 °C)	278.7 ± 11.2

correlation of these cracks with δ-ferrite was made. It has been found in the present study that austenite is stabilized at elevated temperature, as shown in Figures 8c and 8d. The absence of secondary cracking along the δ-ferrite interfaces and appearance of dimples ascertains the requisite of DIM formation for HE under tensile loading, as presented in Figures 6a and 6c. The findings from this study confirms the necessity of deformation-induced martensite transformation on cracking of δ-ferrite interfaces. It is the synergistic effect of hydrogen and DIM that leads to the observed drop in ductility.

At temperatures of 150 °C (>M_d temperature), AISI 321 remains resistant to HE under SSRT, because DIM formation is not favoured. However, for applications operating below the M_d, alloys with a higher nickel equivalent should be prioritized for hydrogen service, as increased austenite stability suppresses martensitic transformation and improves overall HE resistance (Izawa et al., 2019). Additionally, higher nickel/chromium equivalent ratio reduces the δ-ferrite fraction (Soleymani et al., 2015), which may further contribute to improved resistance to HE.

In a previous study conducted by the present authors (Anilkumar et al., 2026), strain-controlled low-cycle fatigue testing at 120 °C in a similar H_2 atmosphere revealed significant hydrogen embrittlement, like that observed at room temperature. Notably, the temperature of 120 °C did not favour the formation of deformation-induced martensite, indicating the embrittlement arises primarily from the presence of δ-ferrite. It should be mentioned that the mechanisms of damage evolution differ substantially between fatigue and monotonic tensile loading. Under cyclic fatigue conditions, damage is highly localized, and is driven by cyclic slip irreversibility, initiation and propagation of crack until failure. In that case, the combination of hydrogen accumulation and strain localization along the δ-ferrite interface boundaries is sufficient to trigger HE, as evidence by crack formation in these sites. In contrast, under monotonic tensile loading, the mere presence of δ-ferrite interface is not sufficient to induce embrittlement, as shown in Figure 6c. Here, the formation of deformation-induced martensite plays a critical role, as it hardens and embrittles a sufficient cross-sectional area of the specimen. This facilitates rapid crack propagation via transgranular quasi-cleavage, and the formation of secondary cracks along δ-ferrite boundaries, as illustrated in Figure 4a. Importantly, HE is influenced not only by temperature but also by mechanical loading conditions. Careful selection of testing methodology based on the application is critical to analyse hydrogen embrittlement susceptibility across a broad range of temperatures.

5. Conclusion

Slow strain rate tensile testing of AISI 321 stainless steel in pressurized hydrogen at room temperature and 150 °C revealed key insights into hydrogen embrittlement. At room temperature, a relative reduction of area (RRA) of 0.44 indicated HE, with fracture surfaces exhibiting transgranular quasi-cleavage and secondary cracking along martensite–δ-ferrite phase boundaries. In contrast, testing at 150 °C showed no signs of embrittlement, as reflected by a high RRA of 0.98 and ductile fracture features such as dimples and Ti(C,N) precipitate pull-out, with no evidence of secondary cracking. These findings suggest that, under the present tensile testing conditions, deformation-induced martensite is a necessity for HE even in the presence of δ-ferrite.

Acknowledgments

The authors acknowledge Siemens Energy for the supply of hydrogen gas tested samples and competence center TechForH2, hosted by Chalmers University of Technology, and financially supported by the Swedish Energy Agency (P2021-90268) and the member companies AB Volvo, Traton AB, Siemens Energy AB, GKN Aerospace Sweden AB, PowerCell AB, Oxeon AB, RISE, Stena Rederier AB, Johnson Matthey AB and Insplorion AB.

Disclosure statement

No potential conflict of interest was reported by the authors.

Funding

This work was supported by the Energimyndigheten (P2021-90268).

References

Anilkumar, V., Wanjura, S., Kulawinski, D., Palmert, F., Ahlström, J., Nyborg, L., & Cao, Y. (2026). Hydrogen embrittlement at elevated temperature during low cycle fatigue of AISI 321 stainless steel. *Engineering Failure Analysis*, *184*, 110307. https://doi.org/10.1016/j.engfailanal.2025.110307

Bachmann, F., Hielscher, R., & Schaeben, H. (2010). Texture analysis with MTEX – free and open source software toolbox. *Solid State Phenomena*, *160*, 63–68. Available at: https://doi.org/10.4028/www.scientific.net/SSP.160.63

Bao, F., Zhang, K., Zhou, Z., Zhang, W., Cai, X., & Zhang, L. (2021). Effect of δ-ferrite on susceptibility to hydrogen embrittlement of 304 austenitic stainless steel in high-pressure hydrogen atmosphere. *Anti-Corrosion Methods and Materials*, *68*(3), 202–208. https://doi.org/10.1108/ACMM-11-2020-2403

Buckley, J. R., & Hardie, D. (1993). The effect of pre-straining and δ-ferrite on the embrittlement of 304L stainless steel by hydrogen. *Corrosion Science*, *34*(1), 93–107. https://doi.org/10.1016/0010-938X(93)90261-E

Choi, D., Nam, J., Moon, B., Saha, S. K., Yoo, J., Park, J. M., … Kang, N. (2024). Effect of δ–ferrite and strain-induced martensite on hydrogen embrittlement of STS 308 L and STS 316 L all-weld metals. *Corrosion Science*, *231*(February), 111977. https://doi.org/10.1016/j.corsci.2024.111977

Frappart, S., Feaugas, X., Creus, J., Thebault, F., Delattre, L., & Marchebois, H. (2010). Study of the hydrogen diffusion and segregation into FeCMo martensitic HSLA steel using electrochemical permeation test. *Journal of Physics and Chemistry of Solids*, *71*(10), 1467–1479. https://doi.org/10.1016/j.jpcs.2010.07.017

Fu, L., Li, Z., Wang, H., Wang, W., & Shan, A. (2012). Lüders-like deformation induced by delta-ferrite-assisted martensitic transformation in a dual-phase high-manganese steel. *Scripta Materialia*, *67*(3), 297–300. https://doi.org/10.1016/j.scriptamat.2012.05.010

Graham, C. D., & Lorenz, B. E. (2018). Delta ferrite is ubiquitous in type 304 stainless steel: Consequences for magnetic characterization. *Journal of Magnetism and Magnetic Materials*, *458*, 15–18. https://doi.org/10.1016/j.jmmm.2018.02.092

Grosse, M., Kalkhof, D., Niffenegger, M., & Keller, L. (2006). Influencing parameters on martensite transformation during low cycle fatigue for steel AISI 321. *Materials Science and Engineering: A*, *437*(1), 109–113. https://doi.org/10.1016/j.msea.2006.04.077

Huang, C., Cai, W., Qi, L., Wang, Z., & Guan, R. (2022). Role of rare-earth yttrium in the hydrogen embrittlement of AISI 321 austenitic stainless steel. *International Journal of Hydrogen Energy*, *47*(87), 37138–37152. https://doi.org/10.1016/j.ijhydene.2022.08.267

Imade, M., Iijima, T., Fukuyama, S., & Yokogawa, K. (2008). Effect of heat-treatment on high-pressure hydrogen gas embrittlement of austenitic stainless steels. *Journal of the Japan Institute of Metals*, *72*(3), 139–145. https://doi.org/10.2320/jinstmet.72.139

Izawa, C., et al. (2019). Relationship between hydrogen embrittlement and Md30 temperature: Prediction of low-nickel austenitic stainless steel's resistance. *International Journal of Hydrogen Energy*, *44*(45), 25064–25075. https://doi.org/10.1016/j.ijhydene.2019.07.179

Jain, A., & Varshney, A. (2024). A critical review on deformation-induced transformation kinetics of austenitic stainless steels. *Materials Science and Technology (United Kingdom)*, *40*(2), 75–106. https://doi.org/10.1177/02670836231212618

Jürgensen, J., et al. (2024). Effect of hydrogen charging on the mechanical properties of high-strength copper-base alloys, austenitic stainless steel AISI 321, Inconel 625 and Ferritic Steel 1.4511.

Kim, Y. S., Bak, S. H., & Kim, S. S. (2016). Effect of strain-induced martensite on tensile properties and hydrogen embrittlement of 304 stainless steel. *Metallurgical and Materials Transactions A*, *47*(1), 222–230. https://doi.org/10.1007/s11661-015-3198-4

Kumar, S. M., & Shanmugam, N. S. (2018). Studies on the weldability, mechanical properties and microstructural characterization of activated flux TIG welding of AISI 321 austenitic stainless steel Studies on the weldability, mechanical properties and microstructural characterization of activat.

Lee, D.-H., Sun, B., Lee, S., Ponge, D., Jägle, E. A., & Raabe, D. (2021). Comparative study of hydrogen embrittlement resistance between additively and conventionally manufactured 304L austenitic stainless steels. *Materials Science and Engineering: A*, *803*(November 2020), 140499. https://doi.org/10.1016/j.msea.2020.140499

Lee, J., Park, C., Park, H., & Kang, N. (2020). Effective hydrogen diffusion coefficient for CoCrFeMnNi high-entropy alloy and microstructural behaviors after hydrogen permeation. *International Journal of Hydrogen Energy*, *45*(16), 10227–10232. https://doi.org/10.1016/j.ijhydene.2020.02.012

Lee, J. A. (2016). "Hydrogen embrittlement. NASA/TM-2016–218602", Shreir's Corrosion, (April), pp. 1–62. https://ntrs.nasa.gov/api/citations/20160005654/downloads/20160005654.pdf

Liu, J., Zhao, M., & Rong, L. (2023). Overview of hydrogen-resistant alloys for high-pressure hydrogen environment: On the hydrogen energy structural materials. *Clean Energy*, *7*(1), 99–115. https://doi.org/10.1093/ce/zkad009

Marchi, C. (2005). Technical reference on hydrogen compatibility of materials. austenitic stainless steels, 304. *Laboratories, Sandia National* (code 2101), 1–18.

Marchi, C. S., et al. (2010). On the physical differences between tensile testing of type 304 and 316 austenitic stainless steels with internal hydrogen and in external hydrogen. *International Journal of Hydrogen Energy*, *35*(18), 9736–9745. https://doi.org/10.1016/j.ijhydene.2010.06.018

Rozenak, P. (1990). Effects of nitrogen on hydrogen embrittlement in AISI type 316, 321 and 347 austenitic stainless steels. 25.

Rozenak, P., & Eliezer, D. (1983). Effects of metallurgical variables on hydrogen embrittlement in AISI type 316, 321 and 347 stainless steels. *Materials Science and Engineering*, *61*(1), 31–41. https://doi.org/10.1016/0025-5416(83)90123-4

Sadeghi, F., Zargar, T., Kim, J. W., Heo, Y.-U., Lee, J. S., & Yim, C. H. (2021). The effect of Ni depletion on athermal martensitic transformation in 304 austenitic stainless steel. *Materials Characterization*, *175*, 111063. Available at: https://doi.org/10.1016/j.matchar.2021.111063

Schindelin, J., Arganda-Carreras, I., Frise, E., Kaynig, V., Longair, M., Pietzsch, T., … Cardona, A. (2012). Fiji: An open-source platform for biological-image analysis. *Nature Methods*, *9*(7), 676–682. https://doi.org/10.1038/nmeth.2019

Soleymani, S., Ojo, O. A., & Richards, N. (2015). Effect of composition on the formation of delta ferrite in 304L austenitic stainless steels during hot deformation. *Journal of Materials Engineering and Performance*, *24*(1), 499–504. https://doi.org/10.1007/s11665-014-1290-3

Stefan, E., Talic, B., Larring, Y., Gruber, A., & Peters, T. A. (2022). Materials challenges in hydrogen-fuelled gas turbines. *International Materials Reviews*, *67*(5), 461–486. https://doi.org/10.1080/09506608.2021.1981706

Wang, Y., Wang, X., Gong, J., Shen, L., & Dong, W. (2014). ScienceDirect Hydrogen embrittlement of cathodically hydrogen-precharged 304L austenitic stainless steel: Effect of plastic pre-strain. *International Journal of Hydrogen Energy*, *39*(25), 13909–13918. https://doi.org/10.1016/j.ijhydene.2014.04.122

Xiuqing, X., Junwei, A., Chen, W., & Jing, N. (2021). Study on the hydrogen embrittlement susceptibility of AISI 321 stainless steel. *Engineering Failure Analysis*, *122*(January), 105212. https://doi.org/10.1016/j.engfailanal.2020.105212

Wang, Y., Wu, X., & Wu, W. (2018). Effect of α′ Martensite Content Induced by Tensile Plastic Prestrain on Hydrogen Transport and Hydrogen Embrittlement of 304L Austenitic Stainless Steel. *Metals*, *8*(9), 660.10.3390/met8090660

Yun, H. S., Jeon, S. K., Lee, Y.-K., Park, J. S., & Nahm, S. H. (2024). Effect of precharging methods on the hydrogen embrittlement of 304 stainless steel. *International Journal of Hydrogen Energy*, *50*, 175–188. https://doi.org/10.1016/j.ijhydene.2023.09.073

Zhang, L., An, B., Fukuyama, S., Iijima, T., & Yokogawa, K. (2010). Characterization of hydrogen-induced crack initiation in metastable austenitic stainless steels during deformation. *Journal of Applied Physics*, *108*(6), 1–5. https://doi.org/10.1063/1.3477321

Zhang, L., Li, Z., Zheng, J., Zhao, Y., Xu, P., Zhou, C., & Li, X. (2013a). Effect of strain-induced martensite on hydrogen embrittlement of austenitic stainless steels investigated by combined tension and hydrogen release methods. *International Journal of Hydrogen Energy*, *38*(19), 8208–8214. https://doi.org/10.1016/j.ijhydene.2013.01.198

Zhang, L., Li, Z., Zheng, J., Zhao, Y., Xu, P., Liu, X., … Li, X. (2013b). Influence of low temperature prestrain on hydrogen gas embrittlement of metastable austenitic stainless steels. *International Journal of Hydrogen Energy*, *38*(25), 11181–11187. https://doi.org/10.1016/j.ijhydene.2013.01.011